A study of the physical, chemical and biological properties of TiO_2 coatings produced by micro-arc oxidation in a Ca–P-based electrolyte

Amanda dos Santos · Joyce R. Araujo · Sandra M. Landi ·
Alexei Kuznetsov · José M. Granjeiro · Lidia Ágata de Sena ·
Carlos Alberto Achete

Abstract In this work, a porous and homogeneous titanium dioxide layer was grown on commercially pure titanium substrate using a micro-arc oxidation (MAO) process and Ca–P-based electrolyte. The structure and morphology of the TiO_2 coatings were characterized by X-ray diffraction, scanning electron microscopy (SEM), transmission electron microscopy, and profilometry. The chemical properties were studied using electron dispersive X-ray spectroscopy (SEM–EDS) and X-ray photoelectron spectroscopy. The wettability of the coating was evaluated using contact angle measurements. During the MAO process, Ca and P ions were incorporated into the oxide layer. The TiO_2 coating was composed of a mixture of crystalline and amorphous structures. The crystalline part of the sample consisted of a major anatase phase and a minor rutile phase. A cross-sectional image of the coating–substrate interface reveals the presence of voids elongated along the interface. An osteoblast culture was performed to verify the cytocompatibility of the anodized surface. The results of the cytotoxicity tests show satisfactory cell viability of the titanium dioxide films produced in this study.

A. dos Santos (✉) · J. R. Araujo · S. M. Landi · A. Kuznetsov ·
J. M. Granjeiro · L. Á. de Sena · C. A. Achete
Divisão de Metrologia de Materiais, Instituto Nacional de
Metrologia, Qualidade e Tecnologia (INMETRO),
Duque de Caxias, RJ 25250-020, Brazil
e-mail: amands1979@gmail.com; asantos@inmetro.gov.br

A. dos Santos · C. A. Achete
Programa de Engenharia Metalúrgica e de Materiais (PEMM),
University Federal do Rio de Janeiro,
Cx. Postal 68505, Rio de Janeiro, RJ 21945-970, Brazil

1 Introduction

Dental implants are frequently the best treatment option for replacing missing teeth, and they help provide good quality of life to edentulous patients [1]. A long-term solution, slow bone loss, and the preservation of nearby healthy tooth tissue are desirable aspects of tooth replacements. Although the osseointegration of implants is considered to be safe and durable, patients with poor bone quality might suffer from bone resorption and biofilm infections. Since the introduction of titanium implants by Branemark more than three decades ago, a number of procedures have been developed to improve their clinical performance [2–4]. The success rate of dental implant therapy is related to the intrinsic capacity of bone for repair. The chemical and surface properties of implants, among other factors, play an important role in improving the osseointegration of the implant–tissue interface [5]. In this context, favourable properties of titanium and titanium alloys are related to the oxide surface layer that forms instantaneously in the presence of oxygen. This naturally formed oxide coating is thin (approximately 3–8 nm in thickness), amorphous, and stoichiometrically defective. It is stable and resistant to corrosion, providing bioinert behaviour after implantation characterized by relatively slow osteogenesis (bone formation). In order to optimize the bone healing time and to achieve long-term stability, improvements in the biological, chemical, and mechanical properties of titanium implants are made by modifying the surface. Many surface modification techniques, such as thermal spraying, sol–gel deposition, ion implantation, and micro-arc oxidation (MAO), have been studied extensively [6–14].

Several approaches have been developed to modify the surface of dental implants and to produce better clinical results, especially in critical situations, such as immediate

load and poor bone quality. In general, the surface changes can be divided into two categories: physical modifications involving moderate roughening of the surfaces and chemical modifications involving a wide range of techniques, such as functionalization, deposition, and chemical etching, which can provide a bioinert surface composed of nano- to microscale structures. Commonly, both approaches are combined to achieve the desired surface characteristics. In recent experiments, calcium (Ca) ion implantation was found to affect the behaviour of bone cells significantly [15]. It was also observed that the Ca ions can attract proteins and growth factors, which are essential for bone formation, and act as binding sites for bone mineral crystals [16]. Han et al. (2003) [12] showed that incorporation of Ca ions in a titanium dioxide (TiO_2) coating has a beneficial effect on bone tissue growth. The TiO_2 coating was produced using a mixture of ß-glycerophosphate (ß-GP) and calcium acetate (CA), and the implants exhibited enhanced adhesion to the bone [17].

Micro-arc oxidation (MAO), or anodic oxidation (AO), is a particularly interesting way of producing ceramic oxide coatings, due to its efficacy, versatility, and cost effectiveness. It is an electrochemical treatment that can change surface topography and chemical composition simultaneously [17, 18]. Another advantage of MAO is the ability to prepare coatings on metal surfaces with complex geometries, such as screw-shape dental implants [19]. The final surface structure and composition are strongly influenced by the electrolyte composition and the conditions of the deposition process. Electrolyte ions are usually incorporated into the coating. Furthermore, the coating properties, such as topography, morphology, porosity, and composition, can vary widely, depending on the different process parameters used [2].

The synthesised titanium dioxide coating can adopt anatase, rutile and, less commonly, brookite crystalline polymorphic forms. The stability or metastability of the TiO_2 crystallographic forms can be tuned by the crystallite size [20]. In nanocrystalline TiO_2, anatase is the most stable phase at ambient conditions, while the nano-rutile polymorph is stable at ambient pressure above 800 °C. Both phases usually coexist at ambient conditions due to a metastability (or stability) of the adjacent phases in the phase diagram. The superior reactivity of the anatase phase seems to be more advantageous for biomaterials applications, such as apatite formation in simulated body fluid (SBF) [21].

The purpose of this study was to investigate how electrolyte ions of a Ca–P-based electrolyte are incorporated into a titanium dioxide coating during MAO. In addition, the morphology, roughness, thickness, structure, chemical composition, and wetting properties of the TiO_2 coating were evaluated. It is well known that the surface properties

strongly affect cellular behaviour [8]. Accordingly, the oxide coatings were investigated to analyse the cell adhesion, spreading, proliferation, cell differentiation, and alkaline phosphatase activity (ALP). The tests were conducted in vitro using osteoblast cells cultured for up to 21 days.

2 Materials and methods

2.1 Sample preparation

Disks of commercially pure titanium (ASTM-Grade 2), 12 mm in diameter and 1 mm in thickness, were used as the substrate. Prior to the anodisation, the samples were ground/polished using up to #1200SiC abrasive papers, cleaned with acetone for 30 min in an ultrasonic bath, and hot-air dried. The samples were anodised in an aqueous solution containing 0.5 mol L^{-1} calcium acetate monohydrate (CaAc, $Ca(CH_3COO)_2 \cdot H_2O$) and 0.02 mol L^{-1} β-glycerophosphate disodium pentahydrate (βGF, $C_3H_7Na_2O_6P$). The MAO process was performed using 150 V DC voltage and 2 A current for 20 s. A 60-Hz pulsed DC power supply was used with an offset voltage of 200 V. The sample produced with this preparation method is referred to as TiO_2–Ca. In order to better investigate the effect of Ca on the physicochemical properties of synthesized TiO_2 coating, a control TiO_2 layer without Ca atoms was prepared using the same synthesis method (MAO) on a geometrically equivalent Ti substrate. The anodisation of the control sample (TiO_2–control) was performed in the electrolyte solution composed of a mixture of phosphoric and sulphuric acids (0.25 mol L^{-1}). The MAO process was performed using 280-V DC voltage and 0.1 A current for 3,600 s. This sample was designated TiO_2–control.

A platinum electrode was used as the cathode (negative) and the titanium disk was used as the anode (positive electrode). The reaction occurred in a water-filled glass jacket system used to minimise overheating during the anodisation. After the MAO treatment, the samples were carefully washed with distilled water and then air-dried.

2.2 Characterization

Scanning electron microscopy (SEM) (Quanta 200; FEI Company, Eindhoven, Netherlands) with energy-dispersive X-ray spectroscopy (EDS) (EDAX Inc., Mahwah, NJ) was used to characterise the morphology of the coatings and to determine the elemental composition in four different regions, using an accelerating voltage of 15 kV. A dual-beam FIB/SEM instrument (Nova Nanolab; FEI Company, Eindhoven, Netherlands) with Pt gas injection system and Omniprobe sample micromanipulator was used to make a

transverse cut in the coating to estimate its thickness and to obtain specimens for the coating–substrate interface analysis. A platinum layer was deposited onto the sample surface to protect it during the FIB milling. The FIB consisted of Ga ions accelerated by a 30 kV voltage against the target.

Transmission electron microscopy (TEM) characterisation was performed using a Cs probe-corrected instrument (Titan 80-300[TM]; FEI Company, Eindhoven, Netherlands) operating at an accelerating potential of 300 kV. Two imaging techniques were used—conventional diffraction contrast TEM and scanning transmission electron microscopy (STEM) using a high-angle dark-field (HAADF) detector. EDS in STEM was used to investigate regions containing amorphous and crystalline nanostructures. Specifically, a coherent, focused probe was raster scanned across the specimen, and at each probe position, the resultant X-ray emission spectrum was recorded. Finally, an elemental map was constructed.

The roughness was measured using a stylus profilometer (DEKTAK 6 M; Veeco, New York, NY). Measurements were collected electromechanically by moving the sample under a 0.7-μm radius diamond-tipped stylus. Each measurement consisted of a sample movement over a 2-mm line for 30 s by a high-precision translation stage at 3-mg stylus force. Three TiO$_2$–Ca samples were analysed, each by ten roughness measurements. The Ra parameter (the arithmetic mean of the deviations of the measured profile from the mean line) was used to characterise surface roughness.

The chemical and phase compositions of the samples were evaluated by X-ray photoelectron spectroscopy (XPS) (ESCAplus P System; Omicron Nanotechnology, Taunusstein, Germany) and X-ray diffraction (XRD) (Bruker AXS, Karlsruhe, Germany). The XPS analyses were performed in an ultra-high vacuum medium using a monochromatic Al Kα = 1,486.7 eV X-ray source with 16-mA emission at a voltage of 12.5 kV. High-resolution spectra were obtained using 40-eV pass energy for calcium, titanium, oxygen, and phosphorous. An argon ion flux was used to sputter the surface in the depth profile measurements. The flux parameters were defined as follows: energy of 3 keV, emission of 17 mA, incidence angle of 45°, and duration up to 100 min. The binding energies were referenced to the carbon 1 s level at 284.6 eV. The Shirley background and a least-squares routine, as implemented in the Casa XPS software (licensed by Omicron Nanotechnology, Taunusstein, Germany), were used for peak fitting.

Raman spectra were acquired with a Horiba T64000 spectrometer (Horiba Instruments Inc., Irvine, CA) equipped with an LN$_{-2}$-CCD operated in micro-single mode with a 600-gr/mm grating. The excitation source was a He–Ne laser (632.8-nm wavelength) with 70-μW (48 W/mm^2)

power at the sample, using a microscope objective of 50x (0.75 NA). The acquired spectra were fitted using a single Lorentzian function for each peak to determine the positions of the peaks and the respective widths.

Symmetric (Bragg–Brentano) and grazing-incidence (0.5° X-ray incidence angle) X-ray powder diffraction patterns of the surfaces were obtained with a Brucker D8-Focus (Bruker-AXS, Karlsruhe, Germany) diffractometer using Cu Kα radiation (Ni filter) with a 2Θ step of 0.02° and acquisition time of 80 s/step. The phase analysis of the coating was performed by the Rietveld method, which is implemented in Topas-Academic software [22].

Fourier transform infrared spectroscopy (FTIR) analyses were performed with a PerkinElmer Spectrum GX spectrometer (PerkinElmer, Waltham, MA) using the potassium bromide (KBr) transmission technique.

The wettability of the coatings was evaluated by measuring the contact angle formed by a droplet (1 μl) at the three-phase boundary (liquid, gas, and solid) intersection using a contact angle goniometer (NRL A-100; Ramé-Hart, Randolph, NJ). Three different types of liquids were used in the tests: distilled water, diiodomethane, and ethylene glycol. Three measurements were performed for each liquid on triplicate TiO$_2$–Ca samples. Each measurement represents an average of 30 measurements taken within 150 s at 5-sec interval. Preliminary in vitro cell viability experiments were performed in triplicate using osteoblast cells on the surfaces. Adhesion of the cells to the surfaces was assessed 4 and 24 h after beginning the tests. The cells were cultured for 14 and 21 days to study their proliferation.

3 Results and discussion

The SEM micrographs (Fig. 1) show the uniform porous morphology of the coating's surface. Visible, interconnected pores were homogeneously distributed over the surface, with no noticeable cracks (Fig. 1a). This type of surface morphology is favourable for osseointegration when a surface is in direct contact with human tissue [19]. Surface properties such as roughness and composition are considered key parameters for altering cell activity. Rough surfaces result in significantly better cell attachment, spreading, proliferation, and differentiation compared to smooth surfaces [8, 23]. Nishimoto et al. [24] showed that serum adhesive proteins preferentially bind to rough surfaces, which have greater surface area compared with smooth surfaces. In this study, the TiO$_2$ coatings had an average roughness value (Ra) of 4.79 ± 0.4 μm and an average thickness of 4.39 ± 0.8 μm.

Lincks et al. [25] studied the effect of titanium surface roughness on cellular response. Two types of finished

(a) **(b)**
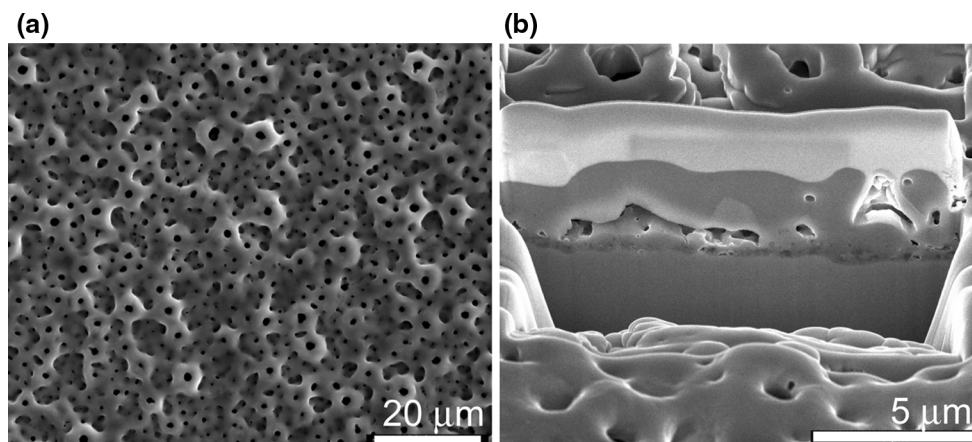
Fig. 1 SEM images of **a** titanium oxide coating topography and **b** cross-sectioned layer–substrate interface

Fig. 2 TEM micrograph of TiO₂–Ca coating: **a** orange cross is crystalline phase and blue cross is amorphous phase; **b** EDS spectra of amorphous and crystalline phases showing O/Ti, P/Ti, and Ca/Ti elemental atomic ratios
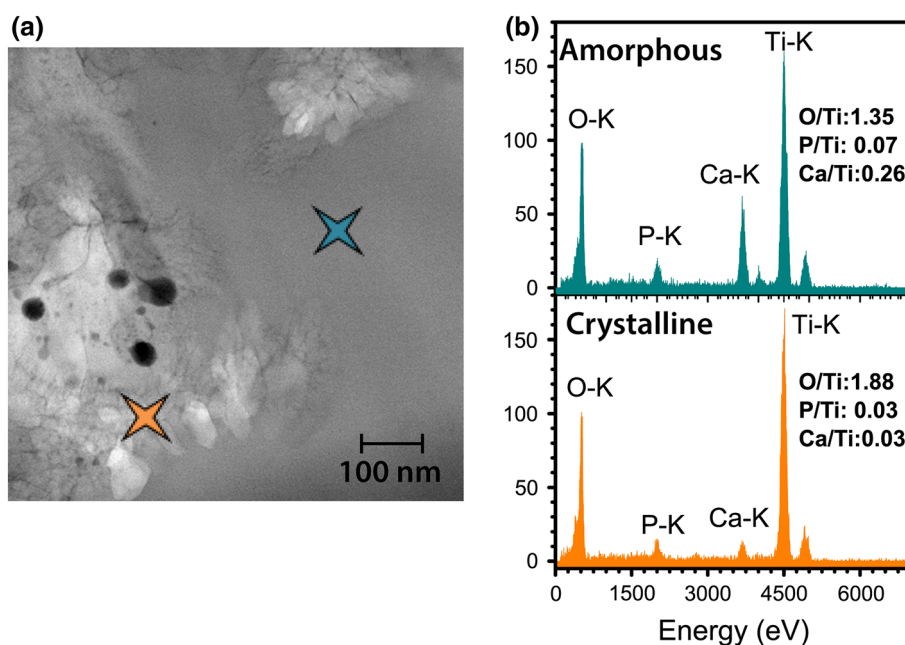

surfaces were used—machined and wet grounded—(Ra up to 4.24 μm), which were machined and fine-polished with a smooth titanium surface (Ra of 0.22 μm). Results of that study demonstrated that rough surfaces enhance cell growth and differentiation, which benefit bone healing.

Figure 1b shows a micrograph of the cross-sectional surface obtained with FIB/FEG-SEM. Despite the presence of elongated voids in the oxide layer, no gaps were observed at the interface between the coating and substrate. Similar results were obtained by Abdullah, who reported subsurface pores near the metal surface and perfect attachment of the TiO₂ coating to the metal surface [21].

Figure 2a depicts a typical TEM micrograph of the oxide layer, showing a mixed microstructure composed of crystalline (light grey cross) and amorphous (black cross) titanium dioxide phases. Figure 2b shows EDS spectra of

the amorphous and crystalline regions marked by black and light grey crosses, respectively, in the STEM image of Fig. 2a. The measured Ca/Ti ratio was higher in the amorphous phase (~ 0.26) than in the crystalline phase (~ 0.03), indicating that calcium atoms tend to concentrate predominantly in the amorphous phase rather than in the crystalline phase. In the case of phosphorous, similar P/Ti ratios were observed in both phases: ~ 0.07 in the amorphous phase and ~ 0.03 in the crystalline phase. It is possible that the low concentration of P ions in the electrolyte (0.02 M C₃H₇Na₂O₆P) favours an even distribution of these atoms in the coating.

The electron diffraction pattern depicted in Fig. 3 shows the presence of anatase and rutile crystallographic polymorphs of titania. This result was confirmed by XRD (Fig. 4a); the powder patterns of the TiO₂–Ca sample
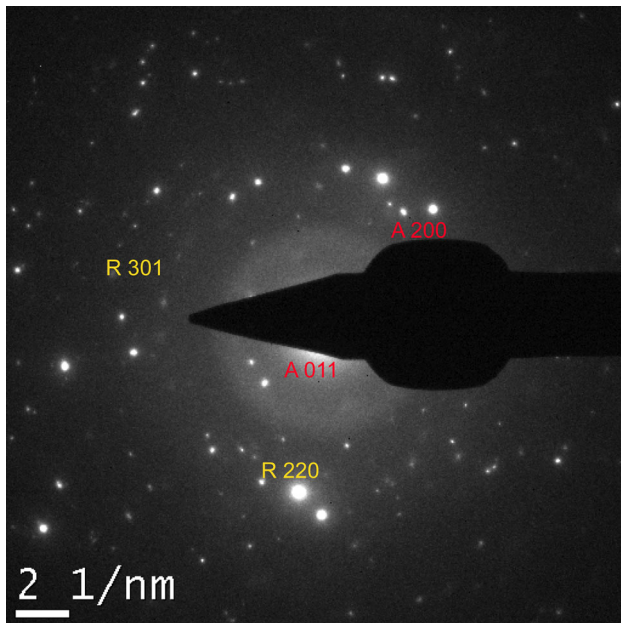
Fig. 3 Electron diffraction pattern of the TiO₂–Ca coating

exhibit diffraction peaks of both the anatase and rutile crystalline phases superimposed on an amorphous background. The diffraction peaks of the titanium substrate vanish in the grazing incidence spectrum (Fig. 4b). Additional weak peaks, which can be seen in the diffraction patterns, can be attributed to minor phases that eventually form during the synthesis. The minor phases cannot be identified due to the low peak intensities and overlap of the minor phase peaks with the anatase and rutile peaks. In distinction to TiO_2–Ca sample, the rutile polymorph was not formed after the synthesis of the TiO_2–control coating (Fig. 4c). This result might indicate that Ca atoms promote the metastabilisation of an otherwise unstable rutile phase in TiO_2 formation. The phase analysis of the TiO_2–Ca sample via the Rietveld method indicated an anatase–rutile weight phase proportion equal to 81:19. The amorphous content in the sample surface can be estimated from the measured relative integrated intensity of the amorphous background (proportional to the respective area in the diffraction pattern). The reference background intensity was obtained using pure Ti substrate measured under the same experimental conditions as the studied TiO_2–Ca sample. The background intensity defined by the Ti substrate approximates the diffuse intensity in XRD patterns coming from scattering processes other than diffraction from the TiO_2–Ca sample. The corrected integrated intensities of the amorphous and crystalline phases in the diffraction pattern of the TiO_2–Ca sample had a proportion of 80:20. The 80 wt% value can be viewed as an estimation of the amorphous content in the coating that most likely incorporates various amorphous phases.

Li et al. [19] also detected an amorphous phase in their titanium oxide surface coating. This amorphous phase was demonstrated by a characteristic diffuse peak in the 20°–30° 2θ range of the XRD pattern. The authors assumed that anodisation with a Ca–P-based electrolyte leads to the formation of amorphous phases in anodic oxide coatings. This conclusion is consistent with the results of other reports on mixed-phase amorphous/crystalline TiO_2 produced by MAO [26, 27].

The obtained Raman spectrum of the TiO_2–Ca sample was dominated by the peaks from the anatase phase (Fig. 5). The assignment of the measured peaks is provided in Table 1. The Raman peak at 439 cm^{-1} can be attributed to the E_g mode of the rutile phase. The same peak, with higher relative intensity, was also observed in the Raman spectrum of the TiO_2–control sample (Fig. 5a). This finding might indicate the manifestation of P atoms, as the TiO_2–control sample did not exhibit a rutile phase in the respective XRD patterns (Fig. 4c). The peak at 592 cm^{-1} that appears as a shoulder of the intense Raman mode at 632 cm^{-1} in both Raman spectra (Fig. 5a, b) cannot be explained by the anatase or rutile phases. This shoulder can be attributed to the effect of P atoms rather than to the effect of Ca atoms, because the same peak is observed in the Raman spectrum of the TiO_2–control sample free of Ca. The comparison of the Raman spectra of TiO_2 samples with and without Ca ions shows slight differences in the positions of the Raman bands, which can be attributed to a chemical factor (Table 1). However, the observed shifts are small (within the measurement uncertainty) and might be caused by other factors, such as different crystallite sizes [28], in addition to differences in chemical composition. The noticeable differences in peak broadening between the two samples, in principle, could be an indirect manifestation of the Ca atoms in the structure of the TiO_2–Ca coating. Morphological properties that affect the width of Raman peaks, such as TiO_2 phase crystallinity, can be related either to Ca-bearing phases formed in the coating or to incorporation of Ca atoms into the TiO_2 structure, where both factors would increase the degree of crystallinity of the TiO_2 phase.

EDS in STEM was used to map the regions containing amorphous and crystalline phases. Selected elemental maps (Fig. 6a–e) show the distribution of the titanium (Fig. 6b), oxygen (Fig. 6c), phosphorus (Fig. 6d), and calcium (Fig. 6e) atoms in the same region of the coating. These images reveal clear trends in the elemental distributions. It can be seen that the calcium content in the amorphous regions is much higher than in the crystalline regions, whereas the phosphorus atoms are distributed more or less uniformly across the entire mapped area. In some works, an increase in the calcium content and a decrease in the phosphorus content has been observed with increasing crystallinity [28–30].

Fig. 4 Selected X-ray diffraction patterns of the TiO$_2$–Ca coating obtained in **a** Bragg–Brentano configuration and **b** grazing incidence geometries. *Asterisks* indicate impurity phases; **c** TiO$_2$–control obtained in Bragg–Brentano configuration
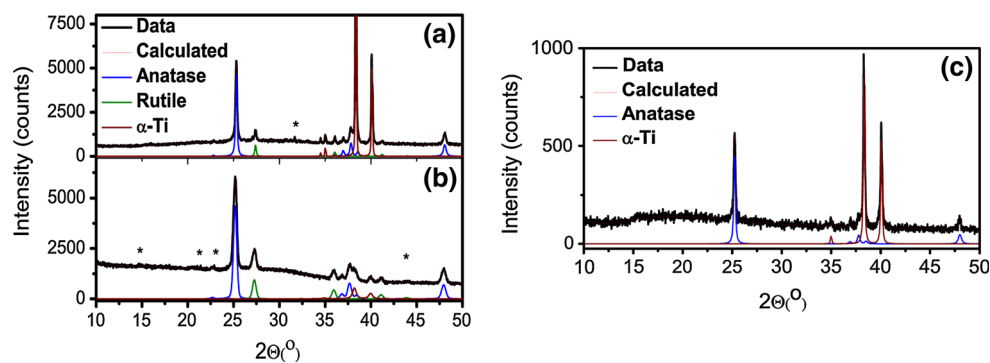
Fig. 5 Raman spectrum of the samples: **a** TiO$_2$–Ca and **b** TiO$_2$–control, showing anatase and rutile phases and effect of the Ca ions on the Raman peak frequencies
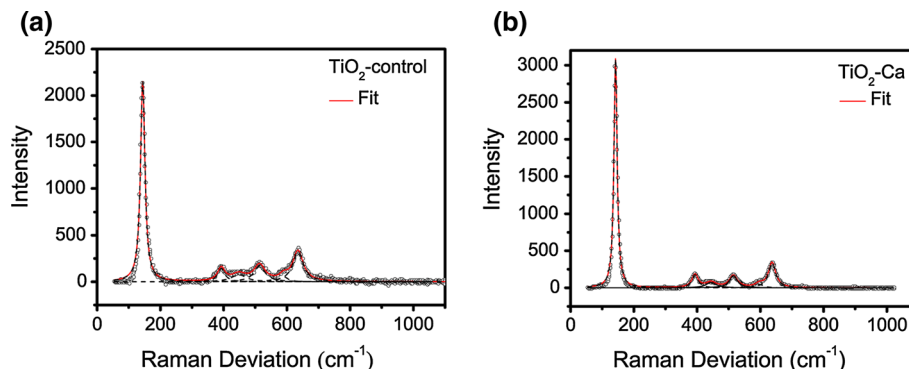
Table 1 Raman results for TiO$_2$–Ca and TiO$_2$–control

Peak number	Peaks assignment (A-anatase, R-rutile)	Position (± 2 cm^{-1})		Width (cm^{-1})		Relative intensity (%)	
		TiO$_2$–Ca	TiO$_2$–control	TiO$_2$–Ca	TiO$_2$–control	TiO$_2$–Ca	TiO$_2$–control
1	$E_{g(1)}^A$, B_{1g}^R	137	140	12.1 ± 0.1	16.8 ± 0.1	100	100
2	$B_{1g(1)}^A$	389	388	24 ± 2	28 ± 4	5.7 ± 0.3	6.5 ± 0.5
3	E_g^R	439	443	40 ± 7	56 ± 14	2.4 ± 0.2	3.6 ± 0.3
4	A_{1g}^A, $B_{1g(2)}^R$	510	509	31 ± 2	42 ± 4	5.3 ± 0.3	8.1 ± 0.4
5	–	592	585	30 ± 9	31 ± 10	1.5 ± 0.3	2.5 ± 0.4
6	$E_{g(3)}^A$, A_{1g}^R	632	630	28 ± 1	40 ± 2	10.9 ± 0.3	15.2 ± 0.4

The depth distributions of the main elements in the coating are shown in Fig. 7a, where the atomic concentrations (at%) are plotted as a function of the sputtering time. The XPS chemical analyses were performed before sputtering and after sputtering durations of 20, 40, 60, 80, and 100 min. Large variations in the concentrations of all atoms were observed up to 40 min of sputtering, which then vanished upon further sputtering, up to 100 min. The carbon concentration showed the higher variation after the sputtering (~ 76–8 %), probably because of the strong adsorption of this element by the pores in the TiO$_2$ surface.

The removal of carbon atoms from the surface by sputtering results in an increase in the relative contents of all elements in the deeper layers of the coating. The overall oxygen content stabilizes at ~ 64 at% for at least 40 min after sputtering, whereas the titanium content becomes constant at ~ 21 at%. The elemental composition remains nearly constant upon further chemical depth profiling. We did not directly control the thickness of the sample during the sputtering process in the XPS measurements. However, indirect qualitative estimation of the sputtered thickness was provided by measuring the carbon atoms. The carbon depth profile is indicative of the sample layer thickness prone to adsorption of other elements. The total sputtering time (100 min) was more than twice the time after which the concentration of carbon atoms stabilises (40 min). Consequently, a sputtering time >40 min is expected to be sufficient to access the deeper layers of the sample, which are free of adsorbed species.
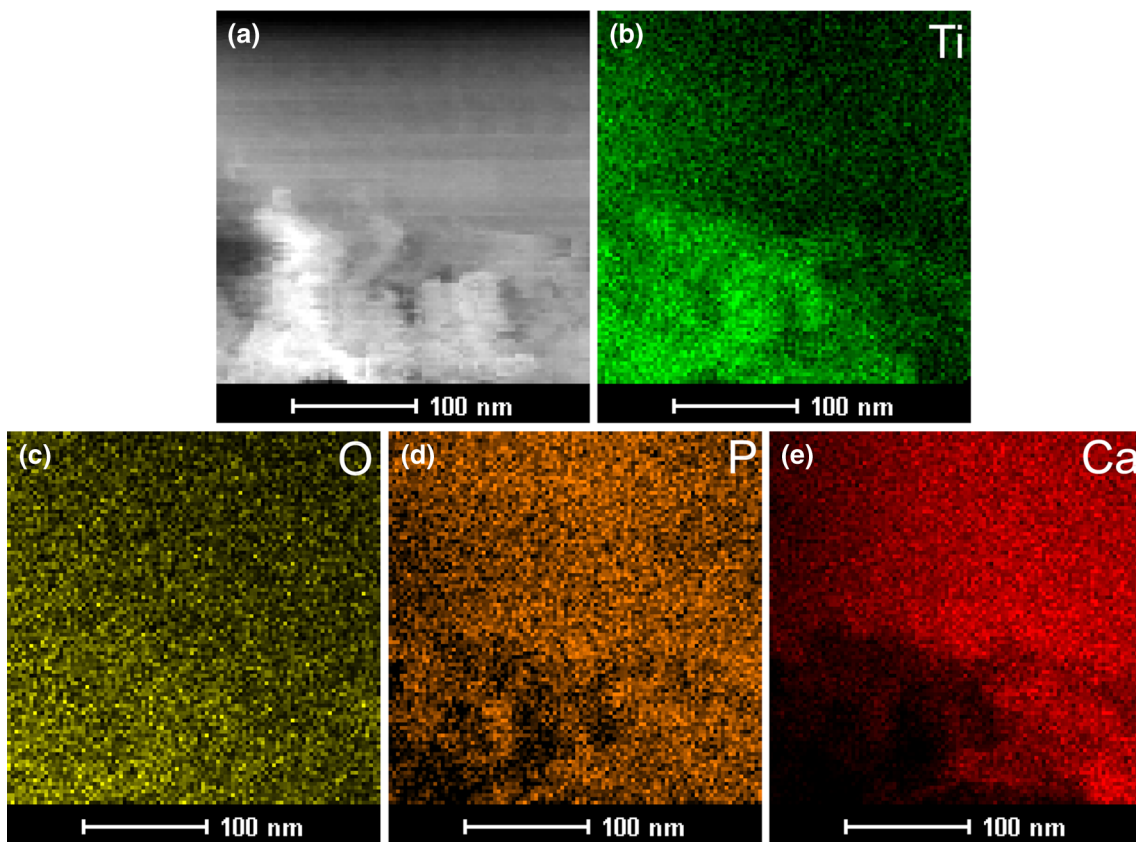
Fig. 6 **a** Cross-section TEM micrograph of TiO$_2$–Ca and chemical elemental maps: **b** titanium, **c** oxygen, **d** phosphorus, and **e** calcium

Fig. 7 **a** TiO$_2$–Ca atomic concentration (at%), calculated from survey XPS spectrum, as a function of sputtering time; **b** XPS survey spectrum of the TiO$_2$ coating showing the chemical elements present in the coating
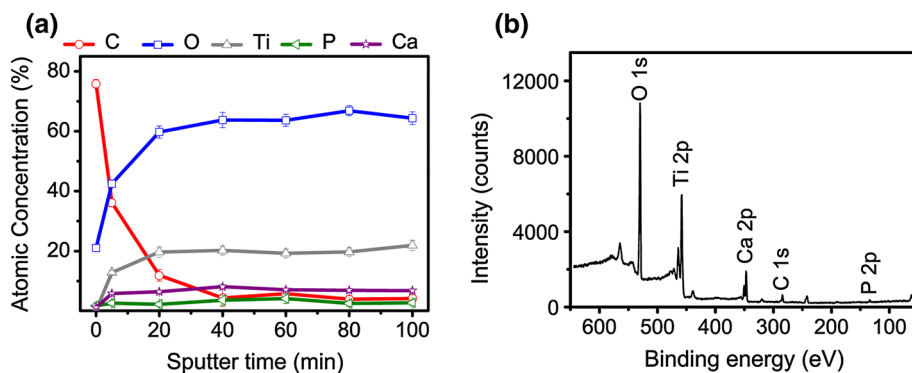
High-resolution XPS spectra of titanium, oxygen, calcium and phosphorous were collected in order to investigate the chemical state of the elements in the coating. Figure 7b presents a typical XPS survey spectrum, which shows the presence of Ti, O, Ca, and P on the surface of the coating. The contents (at%) of each element at the surface were also calculated from survey spectra. Table 2 lists the measured XPS peaks, binding energies (eV), relative atomic percentages, FWHMs (full widths at half-maximum), and chemical groups found in the coating.

The surface was composed of 21 at % of titanium, as determined from the Ti 2p$_{(3/2)}$ core-level binding energy.

Based on the shape of the measured Ti 2p$_{(3/2)}$ peak, it can be deconvoluted into four components (Fig. 8a), corresponding to TiO, TiOH, Ti$_2$O$_3$, and TiO$_2$, analogously to the work of Marino et al. [9]. The peak component corresponding to Ti$_2$O$_3$ has a binding energy of 456.3 eV and accounts for 22 % of the Ti atoms. The TiO$_2$ XPS peak has a binding energy of 457.9 eV and corresponds to 74 % of the Ti atoms, which is the main contribution to the Ti 2p peak of the oxide coating. The peak at 455.1 eV is consistent with TiO (titanium oxide) and/or TiOH (titanium hydroxide), and can be interpreted as either or both compounds. These compounds account for only 4 % of the Ti atoms.

Table 2 Summary of binding energies, contents, FWHM, and assignments of TiO_2–Ca coating calculated from fits of Ca 2p, Ti 2p, and O 1 s high-resolution XPS peaks

| Peak	Binding energy (eV)	Content (%)	FWHM	Chemical group
Ca 2p$_{3/2}$ (1)	346.7	22	1.2	$CaCO_3$
Ca 2p$_{3/2}$ (2)	347.2	78	1.5	$Ca_3(PO_4)_2$, $CaHPO_4$
Ti 2p$_{3/2}$ (1)	455.1	4	2.4	TiO, TiOH
Ti 2p$_{3/2}$ (2)	456.3	22	1.7	Ti_2O_3
Ti 2p$_{3/2}$ (3)	457.9	74	1.4	TiO_2
O 1 s (1)	529.9	75	1.6	TiO_2
O 1 s (2)	531.1	25	2.0	OH, $(PO_4)^{3-}$,CO
P 2p	133.2	100	2.2	$(PO_4)^{3-}$,$(HPO_4)^{2-}$

The doublet with a separation of 3.5 eV in Fig. 8b is consistent with the XPS database lines for the calcium cations. The FWHMs of both peaks in the doublet are approximately 1.5 eV, which corresponds to the calcium atomic content of 7 % at the surface. The peak at 346.7 eV is attributed to $CaCO_3$ (calcium carbonate) and accounts for 22 % of the Ca atoms in the analysed surface. The main peak at 347.2 eV corresponds to $Ca(PO_4)_2$ and $CaHPO_4$ (both calcium phosphates) and is the major contribution (78 %) to the overall Ca 2p$_{3/2}$ peak intensity [31]. The literature data show positive responses of in vitro assays

regarding a beneficial osseointegration role of the calcium and phosphorous present in the coatings [32]. The incorporation of Ca and P in anodic oxide films offers a compositional basis for the formation of calcium phosphates. Calcium phosphate is one of the inorganic phases of hard tissue (bone) and has osteoinductive properties in physiological fluids, making it important in osseointegration [30].

The oxygen 1 s peak in Fig. 8c can be described by two broad components, the first one representing the oxygen atoms coordinated to titanium in TiO_2. The binding energy associated with these oxygen atoms is 529.9 eV, and they account for 75 % of all oxygen in the probed sample volume. This percentage is very similar to that obtained for the titanium atoms (74 %) in TiO_2. The second O1 s peak can be attributed to OH and other oxygen-containing species. For example, the binding energy of 531.1 eV (relative fraction of 25 %) corresponds either to the $(PO_4)^{3-}$ anion in the phosphates or to Ti–OH and CaO species. The high FWHM value of this peak indicates that other oxygen-containing species are also possible, as discussed in the literature [33, 34]. As noted by Abbasi [34], the coatings are exposed to oxygen plasma during the MAO process, and this phenomenon might cause oxygen radicals to attach to the surface.

The measured phosphorous 2p peak (Fig. 8d) is centred at 133.2 eV and corresponds to an atomic content of 2 %. This binding energy indicates that the phosphorous atoms

Fig. 8 High-resolution XPS spectra of TiO_2–Ca showing the fit calculations and chemical groups for the elements: **a** Ti (2p), **b** Ca (2p), **c** O (1 s), and **d** P (2p)
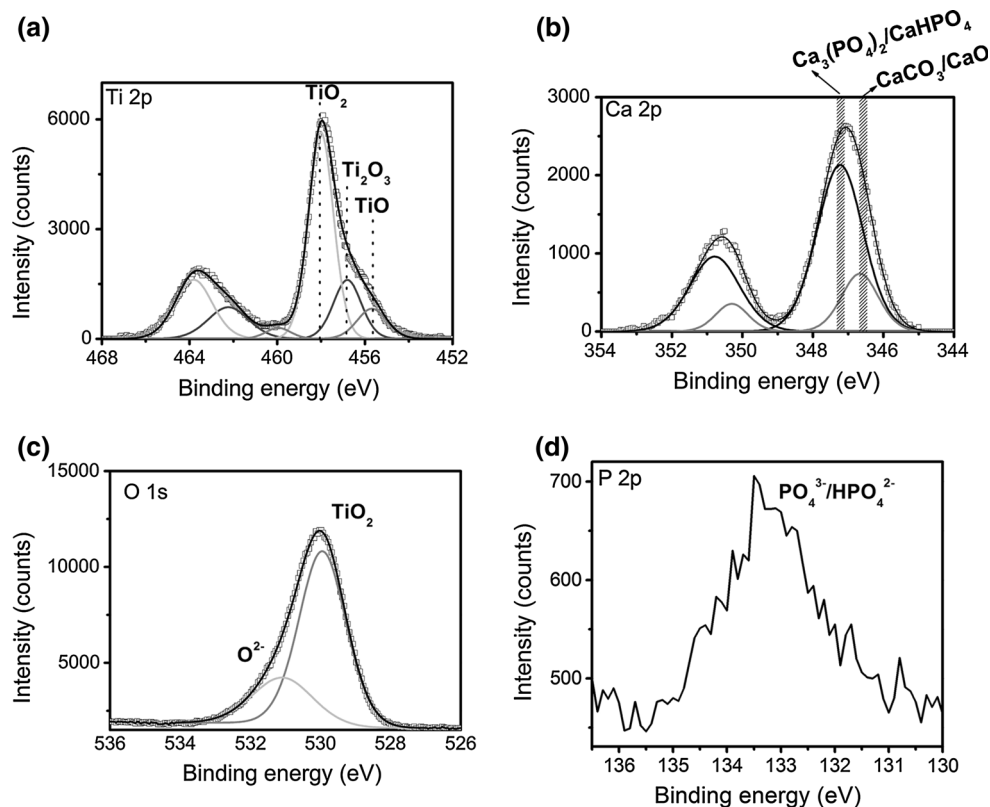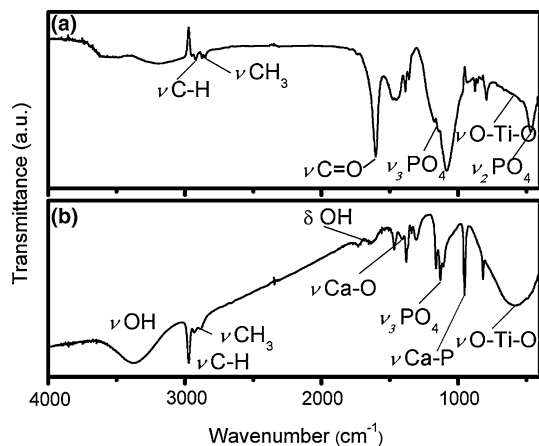
Fig. 9 FTIR spectra of TiO_2 coatings: **a** TiO_2–control sample and **b** TiO_2–Ca. In contrast to the TiO_2–control sample, which essentially shows phosphate, carbonyl, and titanium–oxygen molecular vibrations, the TiO_2–Ca spectrum shows Ca–O, Ca–P, and OH stretching modes

form phosphate ions, $(PO_4)^{3-}$ and $(HPO_4)^{2-}$ [8, 35]. The width of the P 2p peak (FWHM of 2.2 eV) is similar to that obtained by Schreckenbach et al. and Horowitz and Parr [14, 36]. The authors of these studies suggested that the high temperatures of the MAO process increase phosphate condensation, leading to the formation of both phosphate

and pyrophosphate groups. According to Marino et al. [8], the P 2p doublet changes after argon sputtering, and some of the phosphorous atoms have lower binding energies ($\sim$128.5 eV) due to the formation of phosphide species [9, 37]. No phosphide peak was observed in the present study.

The presence of Ca and P ions has been reported to be advantageous for cell growth [38, 39]. The XPS data unambiguously show that calcium phosphates form in the synthesised coating, despite the fact that the respective phases were not detected with XRD (probably because of the amorphous state and/or amounts lower than the experimental detection limit). TEM elemental mapping of the coating supports this result (Fig. 6a–e). The amorphous regions, as confirmed by electron diffraction, contained Ca atoms (the EDS Ca/Ti ratio was 0.26 %), while almost no calcium was detected in the crystalline part of the coating (the EDS Ca/Ti ratio was 0.03 %), as shown in Fig. 2b.

Conclusive evidence of calcium phosphate formation was provided by the FTIR studies. FTIR spectra of the TiO_2–Ca and TiO_2–control samples are shown in Fig. 9. The control sample exhibited bands characteristic of phosphate groups, methylene, and carboxyl species. The carboxyl and methylene groups were probably the result of residual organic species used during the MAO process. The most intense bands were in the regions of 1,740 cm^{-1} (stretching C=O vibration), 1,480 cm^{-1} (stretching CO_3^{2-}), 1,000–1,100 cm^{-1} (ν_3 PO_4^{3-}, asymmetric stretching mode

Table 3 Molecular vibrations modes and their respective assignments obtained from FTIR comparing TiO_2–control and TiO_2–Ca samples [41, 42]

TiO_2–control	TiO_2–Ca	Vibrational mode	Assignment
465	–	ν_2 $(PO_4)^{3-}$	Phosphates
–	583	ν_4 $(PO_4)^{3-}$	Phosphates
400–800	400–800	Stretching	O–Ti–O
790	–	Oscillation mode	H_2O
875	–	Stretching	P–O–C
–	956	Stretching	Calcium phosphates
1,084	1,108	ν_3 $(PO_4)^{3-}$	Phosphates
1,140	1,127	ν_3 $(PO_4)^{3-}$	Phosphates
1,173	1,164	ν_3 $(PO_4)^{3-}$	Phosphates
–	1,305	Asymmetric stretching	C–O–C
1,360	–	Deformation	Carboxyl and methylene groups
1,384	1,385	Bending	CH_3
–	1,415	ν_3 stretching	Ca–O
1,450	1,463	Bending	C–H
1,480	–	ν_3 stretching	CO_3
–	1,634	Bending	O–H
1,740	1,732	Stretching	C=O
2,852	2,877	Symmetric stretching	C–H
2,920	2,931	Asymmetric stretching	C–H
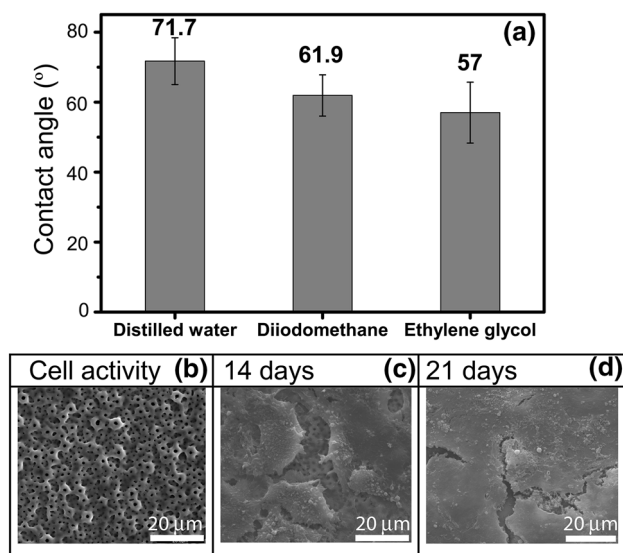
Fig. 10 a Wettability of the TiO₂–Ca coating; **b** SEM image of the surface with no cells; **c** SEM image of the surfaces after 14 days of cellular activity; **d** SEM image of the surfaces after 21 days of cellular activity

of hydroxyapatite), and 875 cm⁻¹ (stretching P–O-C). This sample also showed the presence of H_2O at 1,653 cm⁻¹ (bending mode) and H_2O oscillating motion at 790 cm⁻¹ [40].

The FTIR study of the TiO₂–Ca sample clearly showed characteristic bands of the anatase polymorph of TiO₂. The broad band in the 400–800 cm⁻¹ region of IR spectra is assigned to Ti–O vibrations in TiO₂ lattice [40]. The same broad band of relatively lower intensity overlapped with the vibration mode of phosphate at 465 cm⁻¹ (see Table 3) can be observed in the IR spectrum of the TiO₂–control sample. The obtained FTIR data corroborated the Raman data of this study, indicating higher ordering (crystallinity) of the TiO₂ lattice in TiO₂–Ca sample, which exhibits more pronounced TiO₂ lattice modes. Other bands at 1,463, 1,415, 1,164, 1,000–1,100, and 956 cm⁻¹ observed in the IR spectrum are identified in Table 3 [41]. The presence of calcium phosphates and calcium carbonates in the TiO₂–Ca coating is evident by the appearance of the bands at 956 and 1,415 cm⁻¹, respectively, in agreement with the XPS results of this and earlier studies [32, 43, 44].

As previously mentioned, the surface topography of the coating plays an important role in cell behaviour, such as orientation, shape, and adhesion of the cells on the surface. In general, cell adhesion becomes more favourable with increasing hydrophilicity of the surface, which is another important surface property affecting cell behaviour. The wettability of the coating is determined by measuring the contact angle formed between the solid surface and the liquid/air interface of a droplet. The equilibrium contact

angle is given by Young's equation, $\cos\theta_c = (\sigma_{SV} - \sigma_{SL})/\sigma_{LV}$, where σ_{SV}, σ_{SL}, and σ_{LV} denote the solid–vapour, solid–liquid, and liquid–vapour interfacial energies (surface tension), respectively. This equation describes the thermodynamic equilibrium among the liquid (L), solid (S), and gas/vapour (V) phases [45, 46]. Wenzel showed that Young's equation can apply only when all surfaces are perfectly smooth [47]. In a surface with positive wetting tendency ($\theta_c < 90°$), the roughness enhances this tendency by reducing the contact angle (as should be the case of the studied samples). The measured apparent contact angles of distilled water, diiodomethane, and ethylene glycol on the synthesised TiO₂–Ca coating were below 90°, with respective values of $71.7 \pm 6.7°$, $61.9 \pm 5.9°$, and $57.0 \pm 8.7°$ (Fig. 10a). Consequently, the produced TiO₂–Ca surface was hydrophilic [48], a fact that facilitates protein spreading and cell attachment to the surface [8]. The porous texture of hydrophilic rough surfaces can result in a transition from the Wenzel state of wetting to the Cassie–Baxter [49] state, which is characterised by the formation of a liquid film spreading over the surface beyond the droplet. Such a phenomenon, called hemi-wicking, may occur if the contact angle is below a certain critical value [50]. This critical angle, in turn, depends on the roughness factor of the surface and the dry fraction of wetted surface, connected generally in an intricate manner. The complete imbibition of all drops was observed after 900 s, a fact that suggests a sluggish dependence of the dry fraction of wetted surface on the contact angle that promotes drop spreading.

Based on in vitro cytotoxicity tests, the TiO₂–Ca coating did not appear to be toxic to cells. The cells on the TiO₂ surface spread considerably more on the tested surface regions than on the control surface regions. No significant difference ($p < 0.05$) in ALP activity was observed. Figure 10a shows the surface with no cells and the surfaces after 14 (Fig. 10b) and 21 days (Fig. 10c) of cellular activity. Intense cellular activity can be inferred from these images; the TiO₂ surface features are still visible after 14 days but are completely covered by cells after 21 days, indicating successful cell adhesion and differentiation.

4 Conclusions

In the present study, titanium dioxide films produced by MAO in a Ca–P-based electrolyte formed a homogenous porous layer with no visible cracks. Structurally, the films consisted of crystalline and amorphous phases. The TiO₂ crystalline phases were anatase and rutile. The amorphous phase was mainly composed of TiO₂ and calcium phosphates. Phosphorous was present in both the crystalline and amorphous regions of the samples. XPS analysis confirmed

that Ca and P were incorporated into the film in the form of calcium phosphates $(Ca_3(PO_4)_2/CaHPO_4)$, which might contribute to osseointegration. In addition, the possibility of the adsorption of Ca and P ions could not be discarded. Relevant molecular groups were observed in FTIR and XPS experiments. It is probable that both the adsorption of Ca and P ions and the formation of Ca/P bearing phases occurred during the synthesis of the TiO_2 layer. Raman and XRD measurements showed that Ca incorporation increased the crystallinity of the TiO_2 phase. Contact angle measurements indicated that the anodic surface was hydrophilic and prone to time-dependent superhydrophilicity, which is important for cell adhesion. The synthesised coatings did not exhibit any toxic effects during in vitro cytotoxicity tests.

References

1. Pye AD, Lockhart DEA, Dawson MP, Murray CA, Smith AJ. A review of dental implants and infection. J Hosp Infect. 2009;72(2):104–10.
2. Jackson MJ, Ahmed W. Surface engineered surgical tools and medical devices. 1st ed. New York: Springer; 2007.
3. Takeuchi M, Abe Y, Yoshida Y, Nakayama Y, Okazaki M, Akagawa Y. Acid pretreatment of titanium implants. Biomaterials. 2003;24(10):1821–7.
4. de Sena LA, Calixto de Andrade M, Malta Rossi A, Almeida de Soares G. Hydroxyapatite deposition by electrophoresis on titanium sheets with different surface finishing. J Biomed Mater Res Part A. 2002;60(1):1–7.
5. Lee MH, Park IS, Min KS, Ahn SG, Park JM, Song KY, Park CW. Evaluation of in vitro and in vivo tests for surface-modified titanium by HSO and HO treatment. Met Mater Int. 2007;13(2):109–15.
6. Peláez-Abellán E, Duarte LT, Biaggio SR, Rocha-Filho RC, Bocchi N. Modification of the titanium oxide morphology and composition by a combined chemical-electrochemical treatment on cp Ti. Mat Res. 2012;15(1):159–65.
7. Santos A. Produção de filmes de óxido de titânio por oxidação anódica a microarco. Rio de Janeiro: Dissertação de Mestrado, Universidade Federal do Rio de Janeiro; 2008. p. 97.
8. Zhu X, Chen J, Scheideler L, Reichl R, Geis-Gerstorfer J. Effects of topography and composition of titanium surface oxides on osteoblasts responses. Biomaterials. 2004;25(18):4087–103.
9. Marino CEB, Nascente PAP, Biaggio SR, Rocha-Filho RC, Bocchi N. XPS characterization of anodic titanium oxide films grown in phosphate buffer solutions. Thin Solid Films. 2004;468(1–2):109–12.
10. Yang B, Uchida M, Kim HM, Zhang X, Kokubo T. Preparation of bioactive titanium metal via anodic oxidation treatment. Biomaterials. 2004;25(6):1003–10.
11. de Sena LA, Rocha NCC, Andrade MC, Soares GA. Bioactivity assessment of titanium sheets electrochemically coated with thick oxide film. Surf Coat Technol. 2003;166(2–3):254–8.
12. Han Y, Hong SH, Xu K. Structure and in vitro bioactivity of titania-based films by micro-arc oxidation. Surf Coat Technol. 2003;168(2–3):249–58.
13. Sul YT, Johansson CB, Petronis S, Krozer A, Jeong YS, Wennerberg A, Albrektsson T. Characteristics of the surface oxides on turned and electrochemically oxidized pure titanium implants up to dielectric breakdown: the oxide thickness, micropore configurations, surface roughness, crystal structure and chemical composition. Biomaterials. 2002;23(2):491–501.
14. Schreckenbach JP, Marx G, Schlottig F, Textor FM, Spencer ND. Characterization of anodic spark-converted titanium surfaces for biomedical applications. J Mater Sci Mater Med. 1999;10(8):453–7.
15. Armitage DA, Mihoc R, Tate TJ, McPhail DS, Chater R, Hobkirk JA, Shinawi L, Jones FH. The oxidation of calcium implanted titanium in water: a depth profiling study. Appl Surf Sci. 2007;253(8):4085–93.
16. Fröjd V, Wennerberg A, Stenport VF. Importance of Ca^{2+} modifications for osseointegration of smooth and moderately rough anodized titanium implants—a removal torque and histological evaluation in rabbit. Clin Implant Dent Relat Res. 2012;14(5):737–45.
17. Park IS, Lee MH, Bae TS, Seol KW. Effects of anodic oxidation parameters on a modified titanium surface. J Biomed Mater Res Part B. 2008;84(2):422–9.
18. Frauchiger VM, Schlottig F, Gasser B, Textor M. Anodic plasma-chemical treatment of CP titanium surface for biomedical applications. Biomaterials. 2004;25(4):593–606.
19. Li LH, Kong YM, Kim HW, Kim HE, Heo SJ, Koak JY. Improved biological performance of Ti implants due to surface modification by micro-arc oxidation. Biomaterials. 2004;25(14):2867–75.
20. Navrotsky, A. Energetic clues to pathways to biomineralization: Precursors, clusters and nanoparticles. In: Proceedings of the National Academy of Sciences of the United States of America. 2004, 33rd ed. pp. 12096–101.
21. Abdullah HZ, Sorrell CC. Preparation and characterization of TiO_2 thick films fabricated by anodic oxidation. Mater Sci Forum. 2007;561–565:2159–62.
22. Coelho AA. TOPAS Academic Users Manual, 2005. http://www.topas-academic.net/. Accessed 03 Apr 2014.
23. Cochran DL, Simpson J, Weber H, Buser D. Attachment and growth of periodontal cells on smooth and rough titanium. Int J Oral Maxillofacc Implant. 1994;9(3):289–97.
24. Nishimoto SK, Nishimoto M, Park SW, Lee KM, Kim HS, Koh JT, Ong JL, Liu Y, Yang Y. The effect of titanium surface roughening on protein absorption, cell attachment, and cell spreading. Int J Oral Maxillofacc Implant. 2008;23(4):675–80.
25. Lincks J, Boyan BD, Blanchard CR, Lohmann CH, Liu Y, Cochran DL, Dean DD, Schwarts Z. Response of MG63 osteoblast-like cells to titanium and titanium alloy is dependent on surface roughness and composition. Biomaterials. 1998;19(23):2219–32.
26. Yu S, Yang X, Yang L, Liu Y, Yu Y. Novel technique for preparing Ca- and P-containing ceramic coating on Ti-6Al-4 V by micro-arc oxidation. J Biom Mat Res Part B Appl Biomater. 2007;83(2):623–7.
27. Liu F, Wang F, Shimizu T, Igarashi K, Zhao L. Formation of hydroxyapatite on Ti–6Al–4 V alloy by microarc oxidation and hydrothermal treatment. Surf Coat Technol. 2005;199(2–3):220–4.
28. Swamy V, Kuznetsov A, Dubrovinsky LS, Caruso RA, Shchukin DG, Muddle BC. Finite-size and pressure effects on the Raman spectrum of nanocrystalline anatase TiO_2. Phys Rev B. 2005;71:184–302.
29. Kim KH, Ramaswamy N. Electrochemical surface modification of titanium in dentistry. Dent Mater J. 2009;28(1):20–36.
30. Zhu X, Ong JL, Kim S, Kim K. Surface characteristics and structure of anodic oxide films containing Ca and P on a titanium implant material. J Biomed Mater Res. 2002;60(2):333–8.

31. Zhu X, Kim KH, Jeong Y. Anodic oxide films containing Ca and P of titanium biomaterial. Biomaterials. 2001;22(16):2199–206.

32. NIST-National Institute of Standards and Technology. X-ray photoelectron spectroscopy database, USA. 2013. Available at: http://srdata.nist.gov/xps/. Accessed 15 May 2013.

33. de Souza GB, de Lima GG, Kuromoto NK, Soares P, Lepienski CM, Foerster CE, Mikowski A. Tribo-mechanical characterization of rough, porous and bioactive Ti anodic layers. J Mech Behav Biomed Mater. 2011;4(5):796–806.

34. Yan Y, Sun J, Han Y, Li D, Cui K. Microstructure and bioactivity of Ca, P and Sr doped TiO_2 coating formed on porous titanium by micro-arc oxidation. Surf Coat Technol. 2010;205(6):1702–13.

35. Abbasi S, Bayati MR, Golestani-Fard F, Rezaei HR, Zargar HR, Samanipour F, Shoaei-Rad V. Micro arc oxidized HAp-TiO_2 nanostructured hybrid layers–part I: effect of voltage and growth time. Appl Surf Sci. 2011;257(14):5944–9.

36. Tsutsumi Y, Nishimura D, Doi H, Nomura N, Hanawa T. Difference in surface reactions between titanium and zirconium in Hank's solution to elucidate mechanism of calcium phosphate formation on titanium using XPS and cathodic polarization. Mat Sci Eng C. 2009;29(5):1702–8.

37. Horowitz E, Parr JE. Characterization and performance of calcium phosphate coatings for implants. Philadelphia: ASTM Publication N 04-011960-54, American Society for Testing and Materials; 1994.

38. Roguska A, Pisarek M, Andrzejczuk M, Dolata M, Lewandowska M, Janik-Czachor M. Characterization of a calcium phosphate–TiO_2 nanotube composite layer for biomedical applications. Mat Sci Eng C. 2011;31(5):906–14.

39. Maxian SH, Zawadsky JP, Dunn MG. Effect of Ca/P coating resorption and surgical fit on the bone/implant interface. J Biomed Mater Res. 1994;28(11):1311–9.

40. Feitosa VP, Bazzocchi MG, Putignano A, Orsini G, Luzi AL, Sinhoreti MA, Watson TF, Sauro S. Dicalcium phosphate ($CaHPO_4$–$2H_2O$) precipitation through ortho- or meta-phosphoric acid-etching: effects on the durability and nanoleakage/ultra-morphology of resin-dentine interfaces. J Dent. 2013;41(11):1068–80.

41. Praveen P, Viruthagiri G, Mugundan S, Shanmugam N. Structural, optical and morphological analyses of pristine titanium dioxide nanoparticles—synthesized via sol-gel route. Spectrochim Acta A Mol Biomol Spectrosc. 2014;117:622–9.

42. Socrates G. Infrared and Raman Characteristic Group Frequencies: Tables and Charts. 3rd ed. New York: John Wiley and Sons; 2001.

43. Ohtsu N, Hiromoto S, Yamane M, Satoh K, Tomozawa M. Chemical and crystallographic characterizations of hydroxyapatite- and octacalcium phosphate-coatings on magnesium synthesized by chemical solution deposition using XPS and XRD. Surf Coat Technol. 2013;218:114–8.

44. Ide-Ektessabi A, Yamaguchi T, Tanaka Y. RBS and XPS analyses of the composite calcium phosphate coatings for biomedical applications. Nucl Instrum Meth B. 2005;241(1–4):685–8.

45. Roura P, Fort J. Local thermodynamic derivation of Young's equation. J Colloid Interface Sci. 2004;272(2):420–9.

46. Chow TS. Wetting of rough surfaces. J Phys Condens Mat. 1998;10(27):L445.

47. Wenzel RN. Resistance of solid surfaces to wetting by water. Ind Eng Chem. 1936;28(8):988–94.

48. Coutinho MP, Elias CN. Rugosidade e molhabilidade do titânio usado em implantes dentários com superfícies tratadas. Rev Bras Odontol. 2009;66(2):234–8.

49. Cassie ABD, Baxter S. Wettability of porous surfaces. Trans Faraday Soc. 1944;40:546–51.

50. Bico J, Thiele U, Quéré D. Wetting of textured surfaces. Colloid Surf A. 2002;206(1–3):41–6.